

## Ultrasound intima–media segmentation using Hough transform and dual snake model

Xiangyang Xu<sup>a,1</sup>, Yuan Zhou<sup>a,\*</sup>, Xinyao Cheng<sup>b,2</sup>, Enmin Song<sup>a,3</sup>, Guokuan Li<sup>a,4</sup>

<sup>a</sup> School of Computer Science & Technology, Huazhong University of Science & Technology, 1037 Luoyu Road, Wuhan 430074, PR China

<sup>b</sup> Echocardiographic Laboratory of Cardiovascular Division, Department of Geriatrics, Zhongnan Hospital, Wuhan University, 169 Donghu Road, Wuhan 430071, PR China

### ARTICLE INFO

#### Article history:

Received 17 September 2010

Received in revised form 12 April 2011

Accepted 8 June 2011

#### Keywords:

Ultrasound imaging

Image segmentation

Intima–media thickness

Hough transform

Active contour model

### ABSTRACT

Common carotid artery intima–media thickness (IMT), which is usually measured upon ultrasound images, is an important indicator to cardiovascular diseases. This paper proposes a snake model based segmentation method to automatically detect the boundary of intima–media for IMT measurement. In the proposed method, two contours are initialized from line segments generated by Hough transform and then evolved simultaneously by dual snake model for boundary detection. Experimental results show that the proposed method has strong robustness against ultrasound artifacts, gives better results than traditional snake model and dynamic programming based methods, and achieves similar clinical parameters to ground truth data.

© 2011 Elsevier Ltd. All rights reserved.

### 1. Introduction

Previous researches have indicated that common carotid artery (CCA) intima–media thickness (IMT) is associated with cardiovascular diseases [1,2]. As vascular diseases develop, the structure of intima–media complex (IMC) of vessel wall thickens, which obstructs the blood flow of artery. The slowed blood flow is prone to produce plaques that are unstable and can easily rupture, resulting in the debris transported by blood flow and forming the obstruction of other positions of the artery, which leads to cardiovascular diseases such as stroke and myocardial infarction. Therefore IMT can serve as an important indicator for such diseases at an early stage.

In clinical environment IMT is usually measured from ultrasound imaging because of its non-invasive nature and continually improving quality. Fig. 1 illustrates the structure of IMC in a longitudinal ultrasound image, where the top large image is an example of CCA and the bottom image is the zoomed region of interest (ROI) containing a part of the far wall IMC. It can be observed in the ROI that the lumen, intima, media and adventitia display different echo

patterns from top to bottom. The layers of intima and media are two parallel bands, whose boundary is defined by the lumen–intima interface (LII) and media–adventitia interface (MAI).

Traditional measurement of far wall IMT is based on manual tracing [3]. It suffers from many problems, such as time consuming, demanding experienced experts, different results from different experts or the same expert at different times [4]. The personal experience and subjective judgment from manual tracing could bring a large intra- and inter-observer variability. Computer assisted measurement of IMT has the potential to overcome these problems. The key in this approach is automatic segmentation of IMC in ultrasound carotid artery images, which has also been reported in numerous literatures [4–11].

#### 1.1. Related works

Segmentation in computer vision is usually achieved through minimizing energy functions via variational methods [12–19] and combinatorial methods [20–23]. Variational methods, also known as active contour model, can be traced back to the snake model that defines a parametric contour to locally approximate the boundary of interest [12]. Though several extensions have been made since the original version [13,14,16], its shortcoming of unchangeable topology has not been naturally handled until the application of implicit curve representation, level set [15,17–19]. Variational methods aim to minimize an energy functional in a continuous space so the results can achieve sub-pixel accuracy, while, since they only search the solution in a local manner, an initial estimation of the boundary has to be provided. Contrary to this kind of

\* Corresponding author. Tel.: +86 27 87792212; mobile: +86 13007103358.

E-mail addresses: [xuxy@hust.edu.cn](mailto:xuxy@hust.edu.cn) (X. Xu), [zhouyuanzxcv@gmail.com](mailto:zhouyuanzxcv@gmail.com) (Y. Zhou), [xycheng@whu.edu.cn](mailto:xycheng@whu.edu.cn) (X. Cheng), [esong@mail.hust.edu.cn](mailto:esong@mail.hust.edu.cn) (E. Song), [liguokuan@hust.edu.cn](mailto:liguokuan@hust.edu.cn) (G. Li).

<sup>1</sup> Tel.: +86 13871009617.

<sup>2</sup> Tel.: +86 13971170236.

<sup>3</sup> Tel.: +86 13871254332.

<sup>4</sup> Tel.: +86 13080679046.

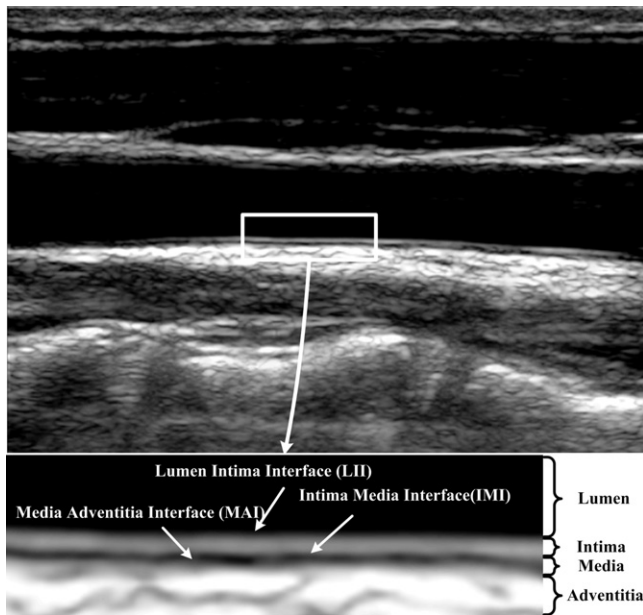


Fig. 1. Illustration of intima-media in a longitudinal ultrasound image.

methods, combinatorial methods use dynamic programming (DP) [20], graph cut [21–23] to minimize a cost function in a discrete space, thus they can only achieve pixel-level accuracy, but the solution obtained is globally optimal. Similar to this classification, the published methods on intima-media segmentation can also be mainly categorized by DP based [4,5,9] and active contour model based [6–8], while a recent detailed review can be found in [11].

The application of DP to this problem was early introduced in Wendelhag et al.'s work [4], and then combined with a multi-scale methodology [5]. In the multi-scale DP, the coarse-scale image was used for estimating the artery wall, which was followed by the detection of far wall MAI and LII in the fine-scale image [5]. Cheng and Jiang pointed out a disadvantage of this DP, that is the searched LII and MAI may cross each other [9]. To overcome this shortcoming, they defined a combined cost function containing both of LII and MAI, as well as a shape constraint relating to their distance range and variation.

On the other hand, an early application of active contour model was made by Cheng et al., who determined the initial contour of LII through connecting two manually selected end points according to image gradient. The MAI was detected by pushing the contour downward from an initial position below the detected LII [6]. Caccarelli et al. detected the LII by searching the boundary point from top to bottom according to image gradient and its fixed left neighbor. The detection of the MAI was achieved by a greedy algorithm, which used an initial contour searched in a region determined by the detected LII [7]. C.P. Loizou et al. used a different order that detected the MAI firstly from an initial contour determined by thresholding and morphological processing and then the LII. The key in their work was to apply image normalization and speckle reduction as a pre-process procedure [8].

However, these active contour based methods have three drawbacks. Firstly, when the first contour fails to approach one side boundary, the error would be accumulated to the second contour. This is especially the case when noise or missing boundary fails the first initialization. Secondly, even if the first detection successfully identifies one side boundary, an estimation of constant thickness cannot guarantee the second initialization close to the desired boundary if the actual thickness deviates far away from the constant estimation. Finally, since the two side boundaries are

detected separately, no shape information connecting the two side contours can be incorporated in their deformation processes [6–8].

## 1.2. Our method

In this paper, we propose an active contour model based intima-media segmentation approach that simultaneously estimates the initial contours for LII and MAI by using Hough transform on partitioned image segments and combines the independent deformations of two contours together by minimizing a unified energy functional. Through imposing distance and angle constraint on the peak searching procedure of Hough line detection and coupling the two independent curves in their evolution, the shape information of two parallel curves with certain distance range is incorporated throughout the method.

Hough transform has been regarded as a robust detection approach for analytic shapes such as lines, ellipses as well as arbitrary shapes [24–27]. Based on the mathematical formulation of the shape, it converts the input binary image to an accumulator array which is a discretized version of the parameter space. The position of the maximum of the accumulator array corresponds to the parameter set of the detected shape in the original image. This technique has been adopted to segment the lumen for longitudinal and intravascular images in [28,29]. However, it is only designed to detect straight or circular lumen boundaries, which is unlike the method in this paper for intima-media boundary detection. Its application here that detects the two nearly parallel line segments in partitioned image segments can adapt to the variability of boundary curve and thickness. Moreover, due to the shape constraint imposed, it is especially robust to ultrasound artifacts such as noises in the lumen or missing boundary.

The active contour model in our method takes a parametric snake model for accurate segmentation because the benefits of implicit contour such as easy to extend to 3D domain and adaptive to topology change are not needed in intima-media segmentation while parametric contour is simple and fast. The proposed active contour model, dual snake (DS) model, couples the evolution of the two curves via forcing their distance at one position being consistent with the neighboring distances to estimate missing boundary of LII. Similar coupled active contour models, both parametric and implicit, have been proposed in other literature [30–34], but they only constrain the between distance or area globally for heart or brain segmentation, which are different from the snake model in this paper that refers to the neighboring distances for missing boundary estimation.

The rest of the paper is organized as follows. Section 2 describes our intima-media segmentation approach in details. Section 3 compares the performances between our method and previous snake or DP based methods, and evaluates our method with respect to clinical parameters. Section 4 discusses the accuracy, efficiency, advantage and limit of our method and concludes this paper.

## 2. Intima-media segmentation

The proposed method accepts a user selected ROI as an input. Fig. 2 shows an overview of the proposed intima-media segmentation approach, which consists of five steps. The first step computes the edge map from the input ROI. The second step thresholds the edge map to a binary image which is later divided horizontally into several equal width non-overlapping binary image segments (BIS). Then for each BIS, Hough transform is used to detect two line segments, primary line (PL) and secondary line (SL), as the approximation to the local LII and MAI. The initial contours for LII and MAI are constructed by sampling the corrected line segments. The

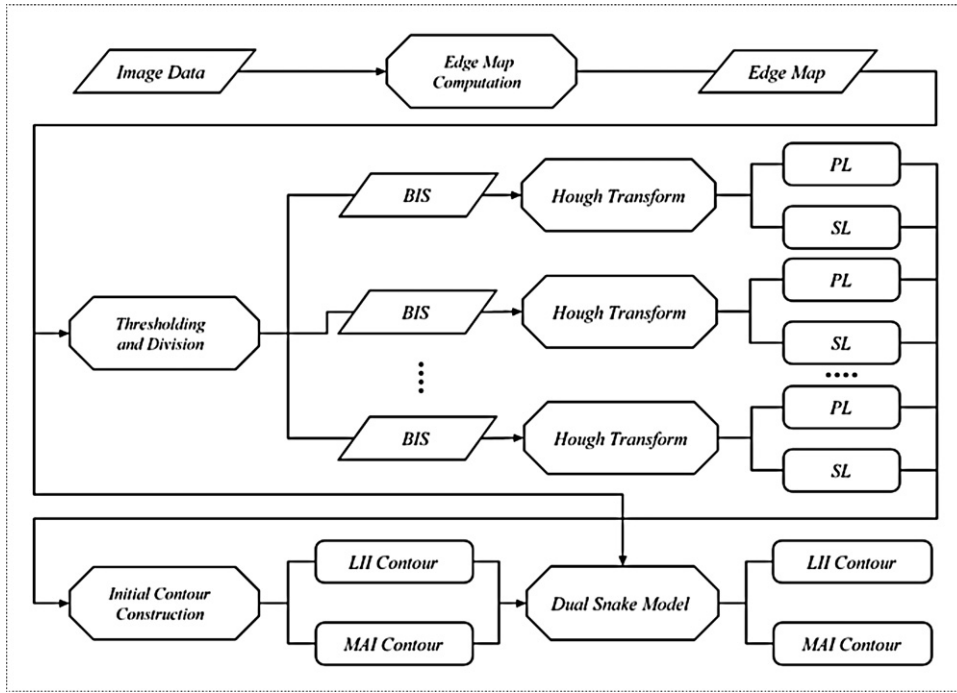


Fig. 2. Overview of our intima-media segmentation approach.

final step applies the proposed DS to evolve the initial contours simultaneously to final segmentation result.

### 2.1. Edge map computation

The edge map is required both for the Hough transform and snake model. It should have large values near the boundary of interested object and can be defined by gradient magnitude of the original image. In ultrasound artery images, LII and MAI have lower echo region above and higher echo region below while IMI has opposite features (Fig. 1). In order to eliminate the interference of IMI, we only consider the edges with positive derivatives with respect to ordinate. The proposed edge map is defined by

$$f(x, y) = \max \left\{ 0, \frac{\partial(G_\sigma * I(x, y))}{\partial y} \right\} \quad (1)$$

where  $I$  denotes the original ROI image,  $\partial/\partial y$  denotes the first derivative with respect to  $y$ ,  $G_\sigma$  is a Gaussian function with standard deviation  $\sigma$ . The effects of our edge map for IMC are illustrated in Fig. 3. We can observe that the edges from the IMI as well as opposite edges in the lumen and adventitia are eliminated in Fig. 3c.

### 2.2. Hough transform

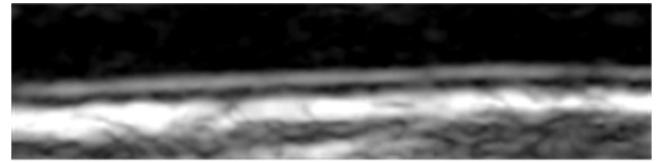
Assuming LII and MAI have piecewise linear boundaries, we can apply Hough transform to detect them upon divided image segments. To be specific, we threshold the edge map  $f(x, y)$  by  $T$ , divide the resulting binary image into  $N_s$  equal width non-overlapping BIS  $\{S_i | i=1, \dots, N_s\}$ , detect two line segments  $PL_i$  and  $SL_i$  as two side boundaries in  $S_i$  by Hough transform, and construct the initial contours for LII and MAI from the sets of  $PL_i$  and  $SL_i$ .

The Hough line detection [24] represents a line by two parameters  $\rho$  and  $\theta$ , where  $\rho$  is the distance between the line and the origin of the coordinate system and  $\theta$  is the orientation of the line. The equation of a line according to the geometry is

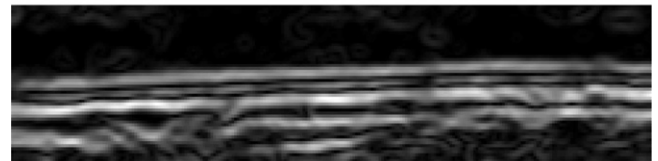
$$\rho = x \cos \theta + y \sin \theta \quad (2)$$

where  $x$  and  $y$  are the coordinates of any point belonging to the line. From (2), the accumulator array  $H(\rho, \theta)$  is constructed in a way through

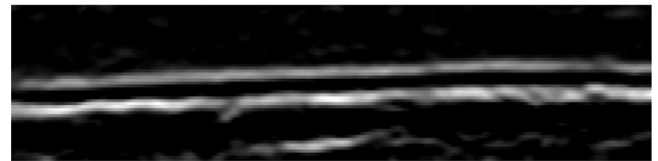
$$H(\rho, \theta) = \sum_k v(x_k, y_k, \rho, \theta) \quad (3)$$



(a)



(b)



(c)

Fig. 3. Comparison between traditional edge map and directional edge map. (a) Original image. (b) Traditional edge map defined by gradient magnitude  $|\nabla G_\sigma * I|$ . (c) Directional edge map obtained by Eq. (1) ( $\sigma = 1$ ).

where  $0 < \rho < L, 0 < \theta \leq \pi, L$  is the diagonal distance of the BIS,  $(x_k, y_k)$  are the coordinates of an edge point and  $v(x_k, y_k, \rho, \theta)$  is a voting function defined by

$$v(x_k, y_k, \rho, \theta) = \begin{cases} 1, & \text{if } \rho = x_k \cos \theta + y_k \sin \theta \\ 0, & \text{otherwise} \end{cases} \quad (4)$$

The construction of accumulator array implies that  $H(\rho, \theta)$  corresponds to the number of a collinear set of edge points in the binary image that are passed through by line  $(\rho, \theta)$ . Hence for each BIS we only need to find two peaks that correspond to the local LII and MAI, respectively.

The first peak can be simply identified by locating the maximum of the accumulator array, i.e., the position  $(\rho_1, \theta_1)$  is defined by

$$(\rho_1, \theta_1) = \underset{(\rho, \theta)}{\operatorname{arg\,max}} H(\rho, \theta) \quad (5)$$

Based on the position of the first peak, we can find a line segment that corresponds to the local boundary. We call it primary line segment (PL), which corresponds to the LII or MAI in our experimental images.

The other side boundary can be detected by finding another peak  $(\rho_2, \theta_2)$  in the accumulator array. We call the corresponding line segment secondary line segment (SL). Here we introduce the shape constraint of IMC. Firstly, the two side boundaries in one BIS of non-plaque region are nearly parallel, so an angle constraint can be imposed between PL and SL, i.e.,  $|\theta_2 - \theta_1| \leq \theta_{\max}$ . Secondly, the distance between them also satisfies the anatomical range, i.e.,  $d_{\min} \leq |\rho_2 - \rho_1| \leq d_{\max}$ . The position of the second peak which corresponds to SL is computed as follows:

$$(\rho_2, \theta_2) = \underset{(\rho, \theta)}{\operatorname{arg\,max}} H(\rho, \theta) \quad (6)$$

where  $(\rho, \theta)$  satisfy the following conditions:

$$|\theta - \theta_1| \leq \theta_{\max} \quad (7)$$

$$d_{\min} \leq |\rho - \rho_1| \leq d_{\max} \quad (8)$$

Fig. 4 illustrates the detection of PL and SL. The number of BIS is determined by  $N_s = \lceil N/l_{\max} \rceil$  given ROI width  $N$ , where  $l_{\max}$  is the maximal length that the width of BIS could achieve. In the experiments, we set  $T=0.3$  for  $f(x, y)$  normalized to 0–1,  $l_{\max}=90$  for partitioning the ROI,  $\theta_{\max}=1$  for forcing PL and SL parallel, and choose  $d_{\min}=5, d_{\max}=25$  according to the actual range of IMT from all experimental images.

### 2.3. Initial contour construction

The above multiple line segments  $\{PL_i | i=1, 2, \dots, N_s\}$  and  $\{SL_i | i=1, 2, \dots, N_s\}$  can be close to the right interfaces if only sufficient boundary edge points exist. However, noise edges and insufficient boundary edge points due to weak boundary could lead to ill-positioned SL. To handle this situation, we correct the ill-positioned one based on its neighboring reference. Assuming that  $PL_i$  and  $SL_i$  are reference pair used for correcting its right neighbor  $SL_{i+1}$ , Fig. 5 shows three possible conditions under which  $SL_{i+1}$  needs correction. That is  $SL_{i+1}$  is too close to  $PL_{i+1}$ , too far away from it or at the wrong side. Note that  $PL_i, SL_i$  and  $PL_{i+1}$  are assumed to be correct approximation to local boundaries, so the left end point of  $PL_{i+1}$  should be close to one of the two right end points of the reference pair. Then we only need to check the adjacent 4 end points between  $S_i$  and  $S_{i+1}$  because the angle constraint in Hough transform makes the two line segments in a BIS nearly parallel. Suppose the ordinates of the 4 points are  $y_a, y_b, y_c, y_d$ , we only need to sort them to obtain the ordered ordinates  $y'_a \leq y'_b \leq y'_c \leq y'_d$  and use the following criterion to determine if correction is needed.

$$y'_c - y'_b < \max\{y'_b - y'_a, y'_c - y'_b, y'_d - y'_c\} \quad (9)$$

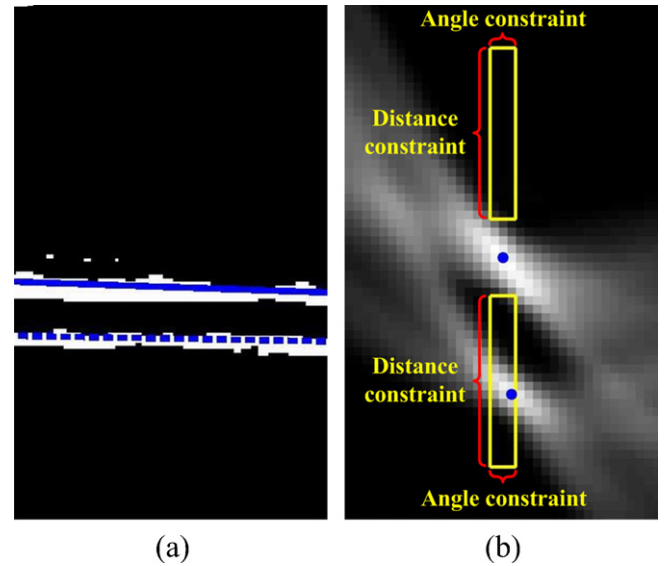


Fig. 4. Boundary detection by Hough transform in a BIS. (a) The blue solid line and dashed line in the BIS correspond to PL and SL, respectively. (b) The middle blue dot is the first peak (corresponds to PL in (a)) of the accumulator array (background image in (b)). The imposed angle constraint and distance constraint restrict the searching region for the second peak to two yellow rectangles below and above the first peak, where the lower blue dot is the searched second peak (corresponds to SL in (a)). (For interpretation of the references to color in this figure legend, the reader is referred to the web version of the article.)

If inequality (9) holds, it means that the central difference of the ordered ordinates is not the largest among the three differences or one of the three conditions in Fig. 5 happens.

Once we are sure that the ill-positioned  $SL_{i+1}$  exists according to its neighboring reference, we can perform its correction by generating a new  $SL_{i+1}$  that is parallel with  $PL_{i+1}$  and making the distance between them equal to the reference distance. The relative position of the new  $SL_{i+1}$ , whether it should be placed above  $PL_{i+1}$  or below  $PL_{i+1}$ , can be determined by the closeness between  $PL_{i+1}$  and the neighboring end points. For example,  $PL_{i+1}$  is closer to the lower reference line segment in Fig. 5, so a new  $SL_{i+1}$  should be placed above  $PL_{i+1}$  with their distance amounting to  $|y_a - y_b|$ .

The above correction step can be started from any  $S_i, i=1, 2, \dots, N_s$  because we do not know which one has the initial line segments corresponding to true boundaries. To overcome this problem, we make a heuristic assumption that makes the pair of  $PL_j$  and  $SL_j$  that passes most edge points in the BIS out of all the pairs as the starting position. Then we can use this pair as reference to correct its left  $SL_{j-1}$  and right  $SL_{j+1}$  (if inequality (9) holds then the correction is needed otherwise no action is performed) and repeat this process that takes the previously corrected pair as reference to correct its left or right neighbor until two ends  $S_1$  and  $S_{N_s}$ . Because the

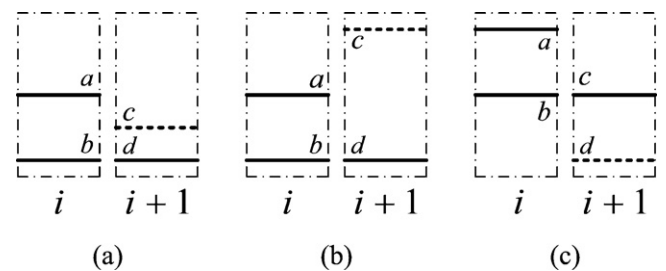
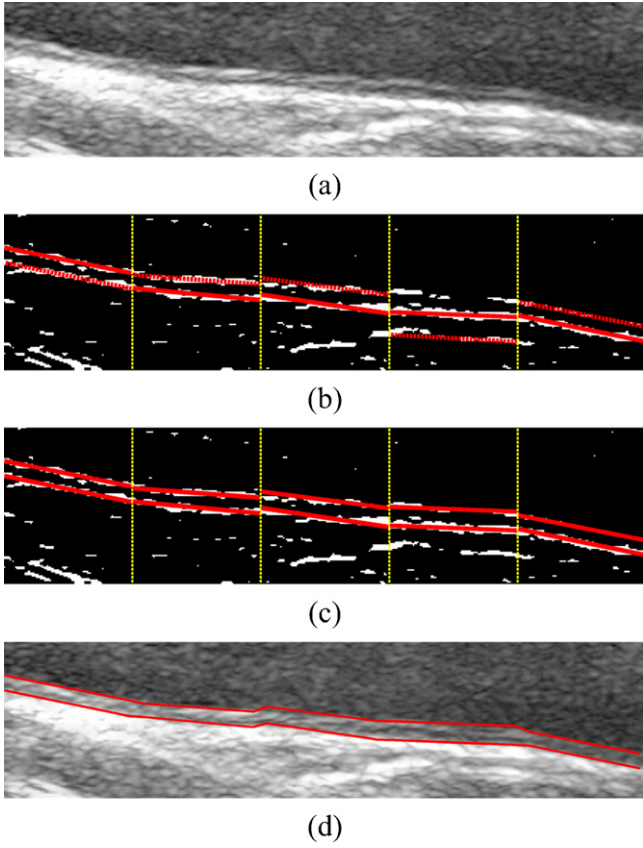


Fig. 5. Three possible cases where  $S_i$  has reference line segments and  $SL_{i+1}$  in  $S_{i+1}$  needs correction. Solid lines (dashed lines) correspond to the line segments that lie at the correct boundaries (false edges). (a)  $SL_{i+1}$  lies close to  $PL_{i+1}$ . (b)  $SL_{i+1}$  lies far away from  $PL_{i+1}$ . (c)  $SL_{i+1}$  lies at the wrong side.



**Fig. 6.** Illustration of correction and sampling processes. (a) Original image. (b) Line segments detected by Hough transform. (c) Corrected line segments. (d) Sampled initial contours. The starting reference pair is in the first BIS from left hand side.

correction is performed according to a strict criterion that checks the ordinates of 4 points, experiments show that only few extreme conditions can cause that to happen and also that if it happens, the following segments are seldom influenced except that they are also ill-positioned. From the corrected line segments, the initial contours are constructed by sampling  $\{PL_i | i = 1, 2, \dots, N_s\}$  and  $\{SL_i | i = 1, 2, \dots, N_s\}$  per 10 pixels and making the higher (lower) sample points as the LII (MAI) contour. The correction and sampling processes are illustrated in Fig. 6.

#### 2.4. Dual snake model

The above initial contours can be driven by snake model for accurate segmentation. Snake model is an edge-based model that attracts the initial contour towards local maxima in the edge map [12]. The traditional snake model finds the curve  $\Gamma(q) : [0, 1] \rightarrow \Omega$  that locally minimizes the following energy functional

$$E_{\text{snake}}(\Gamma) = \frac{w_1}{2} \int_0^1 \left| \frac{\partial \Gamma}{\partial q} \right|^2 dq + \frac{w_2}{2} \int_0^1 \left| \frac{\partial^2 \Gamma}{\partial q^2} \right|^2 dq - \int_0^1 f(\Gamma) dq \quad (10)$$

where  $\Gamma(q) = (x(q), y(q))$ ,  $f(x, y)$  is the edge map.  $w_1$  and  $w_2$  are the weights of curve length and rigidity that control its smoothness.

Previous snake based intima–media segmentation methods use independent deformations for two side contours [6–8]. Recent researches suggest that human vision may interpret the two side boundaries simultaneously and combining the two contours could lead to better results [9,10]. However, such constraint is only incorporated by DP [9] or in the Bayesian framework [10]. We incor-

porate this constraint in the snake model. The modified energy functional is defined by

$$E_{\text{DS}} = E_{\text{int}} + E_{\text{ext}} \quad (11)$$

where  $E_{\text{int}}$  is the internal energy that controls the smoothness of the contours and  $E_{\text{ext}}$  is the external energy that attracts the contours towards boundary. They are defined by

$$E_{\text{int}} = \frac{1}{2} \sum_{i=1}^2 \int_0^1 w_{i1} \left| \frac{\partial \Gamma_i}{\partial q} \right|^2 + w_{i2} \left| \frac{\partial^2 \Gamma_i}{\partial q^2} \right|^2 dq \quad (12)$$

smoothing energy

$$E_{\text{ext}} = \frac{1}{2} \alpha \int_0^1 \left| \frac{\partial(\Gamma_1 - \Gamma_2)}{\partial q} \right|^2 dq + (1 - \alpha) \sum_{i=1}^2 \int_0^1 -f(\Gamma_i) dq \quad (13)$$

uniform energy                      boundary energy

where  $\Gamma_1(q) = (x_1(q), y_1(q))$  is the LII contour,  $\Gamma_2(q) = (x_2(q), y_2(q))$  is the MAI contour.  $w_{11}, w_{12}$  ( $w_{21}, w_{22}$ ) are the weights of length and rigidity of LII (MAI).  $\partial(\Gamma_1 - \Gamma_2)/\partial q$  is the variation rate of the distance vector of corresponding points of the two contours.  $\alpha \in [0, 1]$  adjusts the weight between uniform energy and boundary energy.

Compared to traditional snake model, our improvement focuses on the uniform energy  $\int_0^1 |\partial(\Gamma_1 - \Gamma_2)/\partial q|^2 dq$  in  $E_{\text{ext}}$ . This term makes the distances of the two contours uniform, e.g., two parallel curves have little uniform energy. The uniform energy provides a prior shape constraint, connects the independent deformations together and adjusts the two contours by referring to each other.

$E_{\text{DS}}$  in (11) is a functional with respect to  $x_1(q), y_1(q), x_2(q), y_2(q)$ . To minimize  $E_{\text{DS}}$ , 4 PDE can be obtained by gradient descent flow

$$\frac{\partial x_i}{\partial t} = w_{i1} \frac{\partial^2 x_i}{\partial q^2} - w_{i2} \frac{\partial^4 x_i}{\partial q^4} + \alpha \left( \frac{\partial^2 x_i}{\partial q^2} - \frac{\partial^2 x_{3-i}}{\partial q^2} \right) + (1 - \alpha) \frac{\partial f}{\partial x}(x_i, y_i) \quad (14)$$

$$\frac{\partial y_i}{\partial t} = w_{i1} \frac{\partial^2 y_i}{\partial q^2} - w_{i2} \frac{\partial^4 y_i}{\partial q^4} + \alpha \left( \frac{\partial^2 y_i}{\partial q^2} - \frac{\partial^2 y_{3-i}}{\partial q^2} \right) + (1 - \alpha) \frac{\partial f}{\partial y}(x_i, y_i) \quad (15)$$

where  $i = 1, 2$ . The above parametric contours require frequent re-parameterization because the discretized curve points could bunch or space out [35]. In longitudinal ultrasound CCA images, LII and MAI are nearly horizontal curves that own a unique ordinate per abscissa thus the update of  $x_i(q)$  is not needed. We employ a simplified version that updates only  $y_i(q)$  so that re-parameterization can be avoided. The PDE for evolving the initial contours are defined as follows:

$$\frac{\partial y_i}{\partial t} = w_{i1} \underbrace{\frac{\partial^2 y_i}{\partial x^2} - w_{i2} \frac{\partial^4 y_i}{\partial x^4}}_{\text{smoothing force}} + \alpha \underbrace{\left( \frac{\partial^2 y_i}{\partial x^2} - \frac{\partial^2 y_{3-i}}{\partial x^2} \right)}_{\text{uniform force}} + (1 - \alpha) \underbrace{\frac{\partial f}{\partial y}(x, y_i)}_{\text{boundary force}} \quad (16)$$

where  $y_i(x, t)$  denotes the contour for LII ( $i = 1$ ) or MAI ( $i = 2$ ). The first term is a smoothing force that smoothes the contour, the second term is a uniform force that makes the distances between two contours consistent, and the third term is a boundary force that attracts the contour to edges. We can interpret the uniform force

as an adaptive spring that is affected by its neighboring distances. This force always tries to maintain a uniform distance along the horizontal direction.

In the implementation we employ a semi-implicit scheme similar to [12] that applies an implicit scheme for smoothing force and explicit schemes for uniform and boundary forces. The corresponding difference equations are defined as follows:

$$\mathbf{Y}_i^{n+1} = (\mathbf{A}_i + \mathbf{I})^{-1}[\mathbf{Y}_i^n + \alpha\mathbf{B}(\mathbf{Y}_i^n - \mathbf{Y}_{3-i}^n) + (1 - \alpha)\mathbf{F}_i^n] \quad (17)$$

where  $\mathbf{Y}_i^n = [y_{i,1}^n, y_{i,2}^n, \dots, y_{i,J}^n]^T$  denotes the vector of ordinate of  $J$  discretized curve points at time  $n$ ,  $\mathbf{A}_i$  is a pentadiagonal matrix of 5 diagonals  $w_{i2}, -w_{i1} - 4w_{i2}, 2w_{i1} + 6w_{i2}, -w_{i1} - 4w_{i2}, w_{i2}$  according to implicit scheme,  $\mathbf{B}$  is a tridiagonal matrix of 3 diagonals 1, -2, 1 according to explicit scheme,  $\mathbf{I}$  is an identity matrix of size  $J$ ,  $\mathbf{F}_i^n = [f_y(x_1, y_{i,1}^n), f_y(x_2, y_{i,2}^n), \dots, f_y(x_j, y_{i,j}^n)]^T$  denotes the vector of  $f_y(x, y)$  value of  $J$  discretized curve points at time  $n$ . For parameterization, we sample the contours per 10 pixels with  $w_{i1} = 0.1, i = 1, 2, w_{i2} = 0, w_{22} = 0.1, \alpha = 0.2$  and the magnitude of boundary force field  $|(\partial f / \partial y)(x, y)|$  normalized to 0–1.

The boundary condition  $y_{i,-1}^n, y_{i,0}^n (y_{i,J+1}^n, y_{i,J+2}^n)$  should be chosen carefully for the left (right) end of the contours in the above difference equations. Averaging the neighboring 4 points has been proposed in [6] while this simple approach may not keep slanting ends. To keep the slope of the ends, linear extrapolation can be applied to their centers, i.e., let  $c_{-1}^n, c_0^n$  be the linearly extrapolated values from  $c_1^n, c_2^n, c_3^n, c_4^n$  where  $c_j^n = (y_{1,j}^n + y_{2,j}^n) / 2$ . We also notice that the uniform energy deduces a diffusion term relating to distance. Mirror reflection can be applied to the distance to force the diffusion of distance unbiased by external factors, i.e., let  $d_{-1}^n = d_3^n, d_0^n = d_2^n$  where  $d_j^n = y_{2,j}^n - y_{1,j}^n$ . The illustration of this boundary condition for the left end is given in Fig. 7.

### 3. Results

Fig. 8 shows two difficult segmentation tasks and our results. In Fig. 8a, strong noises are present in the lumen. The proposed method overcomes such noises in Fig. 8c and e. Hough transform reduces the interference by considering all the edge points in a BIS.

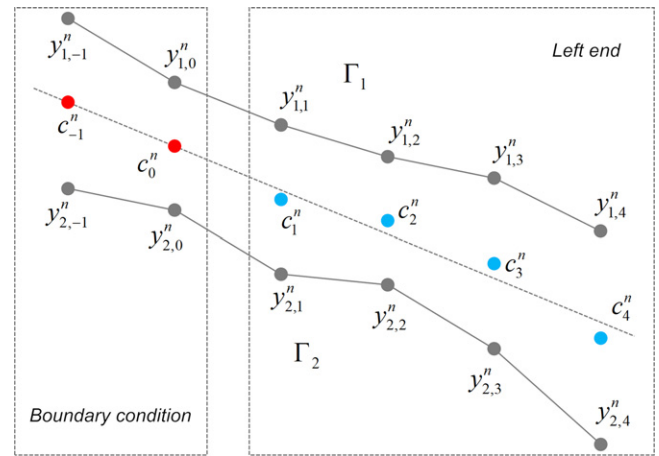


Fig. 7. Illustration of boundary condition for dual snake model. The centers  $c_{-1}^n, c_0^n$  are the linearly extrapolated values from  $c_1^n, c_2^n, c_3^n, c_4^n$  to keep slanting ends. The distances satisfy  $d_{-1}^n = d_3^n, d_0^n = d_2^n$  in accordance with the diffusion term of distance.

The missing boundary in Fig. 8b may complicate the initial contour estimation and attract the two side contours to the same interface while the proposed method estimates the missing boundary in Fig. 8d and f. The constraints in Hough transform and the uniform energy in DS both contribute to this success.

#### 3.1. Data acquisition

Our experimental images came from a Philips iE33 ultrasound system with an 11M probe, in Zhongnan Hospital of Wuhan University, Wuhan, China. All the images were logarithmically compressed and recorded digitally on an optical disk with 256 gray levels. The subjects were 25 patients, including 16 male and 9 female, who received ultrasonographic examination in Zhongnan Hospital when their ages ranged from 17 to 86 years with a mean of 57 years. We selected 50 ROI images for experiments, 1–3 images for each patient, with average ROI size  $308 \times 67$  pixels ( $19.8 \text{ mm} \times 4.3 \text{ mm}$ ). In the examination of 22 subjects, the IMT

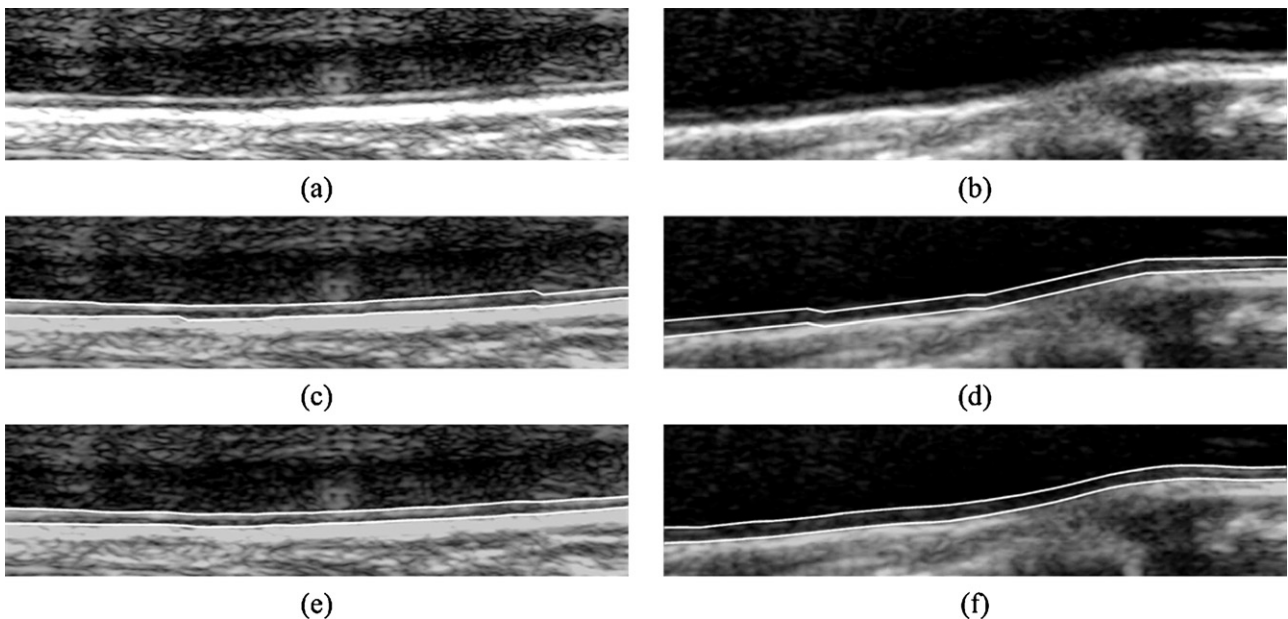
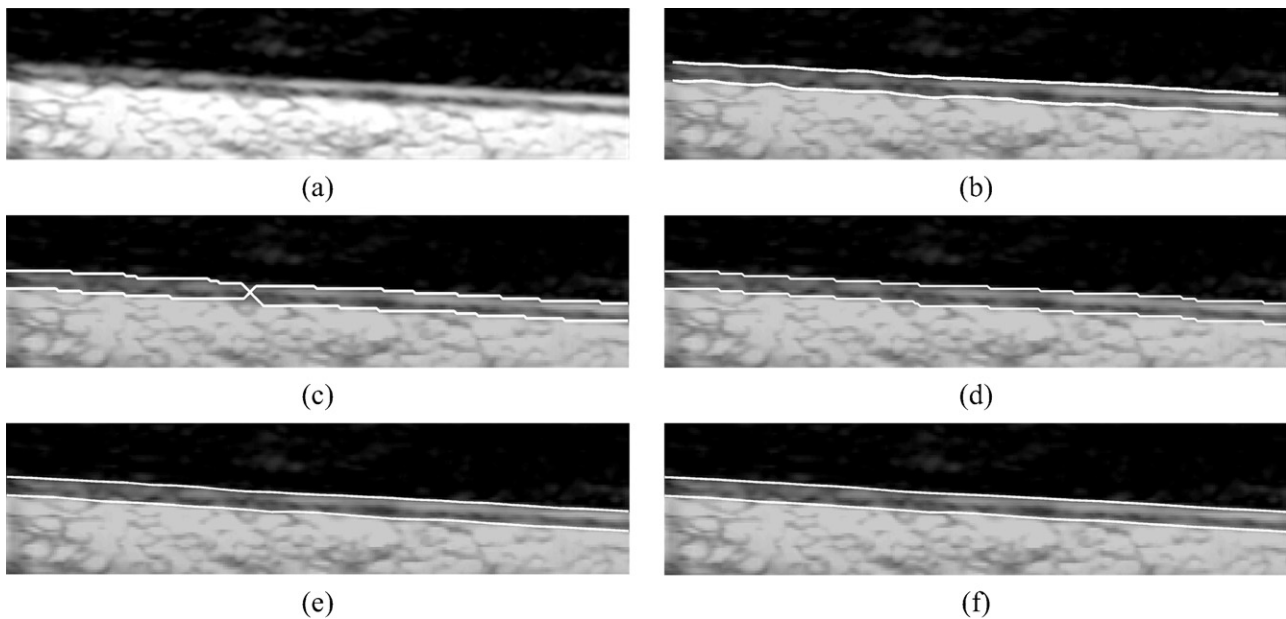


Fig. 8. Two examples of segmentation results against severe artifacts. (a) An image with strong noises in the lumen. (c and e) The initial contours and final evolution contours from (a), respectively. (b) An image with missing boundary of LIL. (d and f) The initial contours and final evolution contours from (b), respectively.



**Fig. 9.** Comparison between our method and previous methods for a thin IMC. (a) The original image. (b–f) Contours generated by gold standard (b), TDP (c), DDP (d), TS (e) and our method (f), respectively.

was less than 1 mm and no visible plaque was detected. In order to validate our method in the case of large IMT, we also included atherosclerotic subjects with visible plaque existing. However, in this situation, overt region of plaque was excluded and only non-plaque region of the original image was selected for analysis.

### 3.2. Quantitative metric

To evaluate the accuracy of the automatic methods, we compared them with gold standard established by the experts who manually delineated each side boundary totally 4 times for each image. The gold standard was obtained by averaging the 4 interpolated matched points (ordinates) of manual contours. To measure accuracy of the automatic methods, mean absolute distance (MAD) between gold standard and automatic segmented contour was calculated. Suppose the ordinate of gold standard is  $y_{GS}$  and that of the matched point of automatic method is  $y_{AM}$ , the MAD is defined by

$$MAD = E(|y_{GS} - y_{AM}|) \quad (18)$$

For each ROI, the physical pixel size was retrieved from the original image to compute the MAD in physical unit.

### 3.3. Comparison with previous methods

We compared our method with traditional snake (TS) model and DP based segmentation methods. TS can be regarded as removing the uniform energy in (13), i.e., setting  $\alpha=0$ , if we employ the same proposed initial contour construction procedure. Traditional Dynamic Programming (TDP) for intima–media segmentation searches two side boundaries separately using the same cost function [9]. Based on the first searched boundary, the other side boundary is searched after inhibiting the edge map according to the range of IMT. The optimal weight of smoothness  $\kappa$  is searched by minimizing the mean of errors of all interfaces with step 0.01. Dual Dynamic Programming (DDP) is an improved DP based approach that combines the two independent cost functions together in a unified framework such that a smooth distance term and hard constraints can be incorporated [9]. The optimal parameters for smooth distance term  $\lambda_1$  and smooth curve term  $\lambda_2$  are

searched in the 2-D parameter space with step 0.02 to minimize the same criterion.

Fig. 9 illustrates a comparison between our method and previous methods for a thin IMC. The segmentation results indicate that all the methods produced contours close to boundaries and similar to gold standard except TDP. This may be explained by the inconsistent boundary strength and small IMT. Because the left part of this image features a strong boundary for MAI whereas the right part features a strong boundary for LII, the first searched contour by TDP has its left part attracted to the MAI and right part attracted to the LII, which has the error accumulated to the second contour that crossed the first one. Note that such error can be eliminated by increasing the weight of smoothness  $\kappa$  for TDP. However, such adjustment would cause other problems since the parameter is searched to satisfy all the images as much as possible.

Fig. 10 illustrates a comparison for a slanting IMC with weak boundary. We can observe that both TDP and DDP failed in this context. On the contrary, TS and our method succeeded because of the same initial contour construction they applied. The bad contours generated by DP based methods may be attributed to the slanting weak boundary. Because of the large smoothness term imposed, TDP and DDP are inclined to produce horizontal contours instead of slanting ones. Moreover, the weak boundary did not suffice to attract the contours, which resulted in the right parts of the contours horizontally away from the true boundaries. We also note that a small smoothness term would make them succeed to segment the IMC. However, such adjustment would cause other problems because the parameters are searched to minimize the mean of MADs of all boundaries.

Fig. 11 illustrates a comparison for an IMC with missing boundary caused by low gain setting when the image was recorded. We find that DDP and our method produced similar contours to gold standard while TDP and TS had the two contours attracted to the same interface. The successes of DDP and our method can be attributed to the smooth distance term and the uniform energy, respectively, which estimated the missing information from the MAI contour and neighboring distances. Without this constraint, both TDP and TS that feature separate boundary detections failed to produce a proper LII contour.

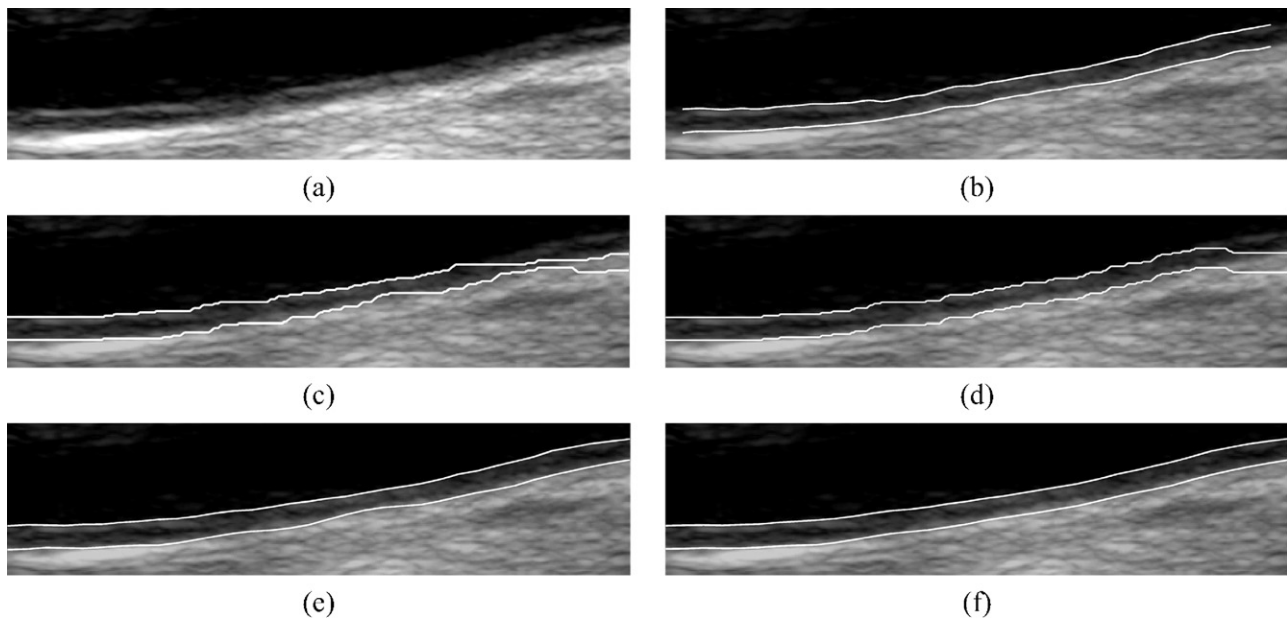


**Fig. 10.** Comparison between our method and previous methods for a slanting IMC with weak boundary. (a) The original image. (b–f) Contours generated by gold standard (b), TDP (c), DDP (d), TS (e) and our method (f), respectively.

Table 1 shows the statistics of segmentation errors of all the methods and Fig. 12 uses the box plots to visualize their distribution. It can be observed that the snake based methods have less overall error than DP based methods. This may be explained by our robust initial contour construction employed by snake based methods. Although the DP based methods have fewer parameters to adjust, we find that these parameters are unstable and sensitive to boundary slope. Given proper generated initial contours, the snake based methods have the ability to achieve better segmentation results. Another phenomenon is that the proposed DS performed slightly better than TS. This advantage has been visualized in the box plot showing the large extreme error of TS in Fig. 12a. Recall that without the uniform energy the LII contour was

**Table 1**

Segmentation errors of all the methods in our experiments.<sup>a</sup>

MAD ( $\mu\text{m}$ )	LII (Mean $\pm$ SD)	MAI (Mean $\pm$ SD)	IMC (Mean $\pm$ SD)
TDP <sup>b</sup>	47.0 $\pm$ 46.6	63.3 $\pm$ 38.7	55.2 $\pm$ 40.4
DDP <sup>c</sup>	38.2 $\pm$ 17.1	53.1 $\pm$ 26.2	45.6 $\pm$ 19.4
TS	29.5 $\pm$ 23.0	49.0 $\pm$ 24.5	39.3 $\pm$ 20.4
Our method	29.0 $\pm$ 15.0	47.1 $\pm$ 23.0	38.1 $\pm$ 16.4

<sup>a</sup> The number of images is  $n = 50$ .

<sup>b</sup> The optimal parameter  $\kappa$  for TDP is set to be  $\kappa = 1.05$ .

<sup>c</sup> The optimal parameter set for DDP is  $\lambda_1 = 1.34$ ,  $\lambda_2 = 0.42$ .

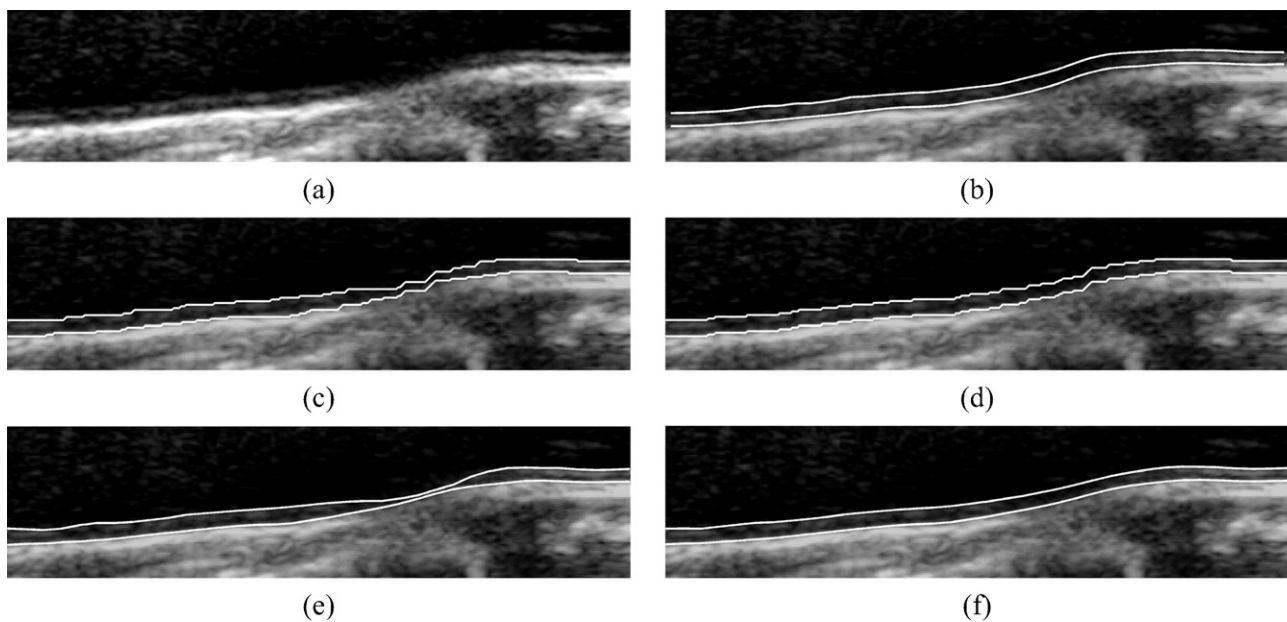


**Fig. 11.** Comparison between our method and previous methods for an IMC with missing boundary. (a) The original image. (b–f) Contours generated by gold standard (b), TDP (c), DDP (d), TS (e) and our method (f), respectively.

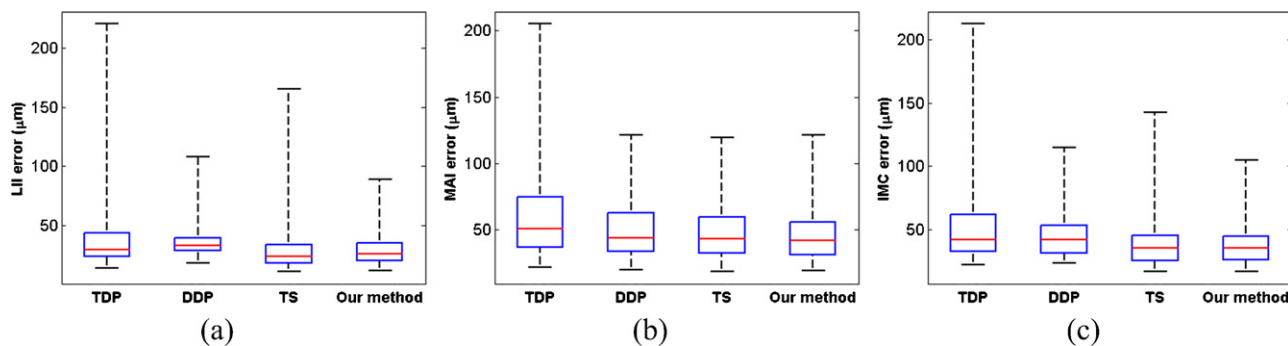


Fig. 12. Box plots of segmentation errors among TDP, DDP, TS and our method. (a) LII error. (b) MAI error. (c) IMC error.

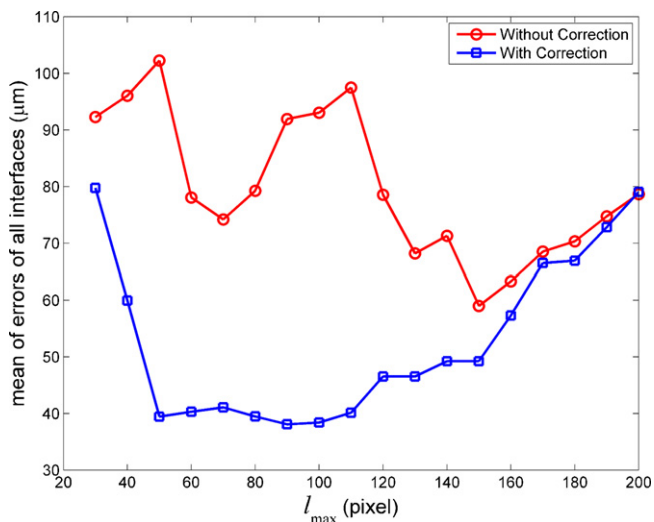


Fig. 13. Parameter sensitivity analysis of  $l_{\max}$  for both correction and non-correction procedures in the initial contour construction.

attracted to the MAI when missing boundary was present, which may account for such benefit.

#### 3.4. Parameter sensitivity analysis

The maximal BIS width  $l_{\max}$  is important to the proposed method whose basic assumption is that the boundary curve can be approximated using piecewise linear representation. Fig. 13 shows different overall performances from different  $l_{\max}$ , both with and without correction procedure in the initial contour construction, where the ordinate is the mean of errors of IMC of all experimental images based on the abscissa  $l_{\max}$ . We can see that the correction procedure in the initial contour construction worked very well such that the overall error with correction is much lower than that without correction. Moreover, we find the performance with correction is rather stable even when  $l_{\max}$  lies in a wide range [50, 110], in which the overall error is still lower than that of DP based methods according to Table 1. However when  $l_{\max} < 50$  or  $l_{\max} > 110$  the performance decreases dramatically. The large error from  $l_{\max} < 50$  can be explained by that the proposed method relies on the PL cor-

responding to one side boundary whereas small width of BIS does not guarantee this assumption due to insufficient local edge point information. The same failure occurs when  $l_{\max} > 110$ , which suggests that the boundary curve could be complicated and cannot be approximated using a small number of long line segments.

#### 3.5. Clinical evaluation

To evaluate our method in clinical environment, we calculated the thicknesses of corresponding point pairs between two side contours. For each image, mean and max value of IMT can be obtained from these thicknesses. We computed the mean and standard deviation (SD) of these statistical variables for gold standard, our method and the difference between. Table 2 shows the comparison of  $IMT_{\text{mean}}$  and  $IMT_{\text{max}}$  between gold standard and our method. It can be seen that these two methods generate similar statistics. However, the SD of difference of  $IMT_{\text{mean}}$  is less than that of  $IMT_{\text{max}}$ , which implies that  $IMT_{\text{mean}}$  is more reliable than  $IMT_{\text{max}}$  from our method. This may be explained by the fact that the uniform energy tends to obliterate minor details. The precise results indicate that the error of  $IMT_{\text{mean}}$  lies between  $-0.03$  mm and  $0.08$  mm and that of  $IMT_{\text{max}}$  lies between  $-0.1$  mm and  $0.09$  mm within 95% confidential interval. Fig. 14a plots the  $IMT_{\text{mean}}$  by our method versus gold standard. The slope of the linear regression line is 1.09. Fig. 14b is the Bland–Altman plot [36] of  $IMT_{\text{mean}}$  between our method and gold standard.

## 4. Discussion and conclusion

### 4.1. Accuracy and efficiency

The results in Table 1 and Fig. 12 show that the average errors and median errors of LII and MAI are all within  $50 \mu\text{m}$ , which are similar to the results reported in the review [11]. However, the accuracy of MAI is lower than that of LII. This may be attributed to the ambiguous boundary understanding of MAI (especially large IMT) from experts who did not delineate the contours according to gradient maxima. This problem has also been mentioned in reference [5] that suggests handling it through incorporating into the cost function multiple features determined by a complex training procedure. The side effects of the relative large MAI error also include the larger  $IMT_{\text{mean}}$  of our method compared to gold

Table 2  
Comparison of mean and max value of IMT between gold standard and our method.<sup>a</sup>

	Gold standard (Mean $\pm$ SD)	Our method (Mean $\pm$ SD)	Difference (Mean $\pm$ SD)	R
$IMT_{\text{mean}}$ (mm)	$0.63 \pm 0.14$	$0.65 \pm 0.16$	$0.02 \pm 0.03$	0.99
$IMT_{\text{max}}$ (mm)	$0.75 \pm 0.16$	$0.75 \pm 0.18$	$-0.00 \pm 0.05$	0.97

<sup>a</sup> The number of images is  $n = 50$ .

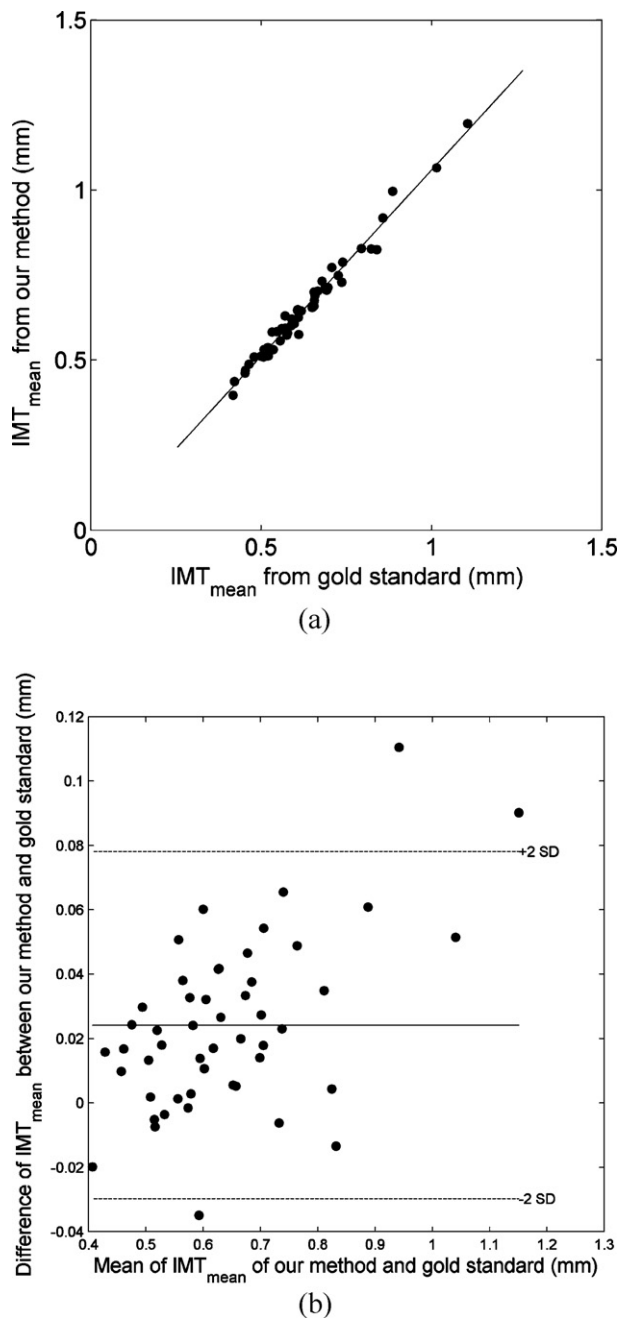


**Fig. 14.** Statistical evaluation of  $IMT_{mean}$  between our method and gold standard. (a)  $IMT_{mean}$  from our method versus  $IMT_{mean}$  from gold standard. (b) Bland–Altman plot of  $IMT_{mean}$  between our method and gold standard.

standard as shown in Table 2. Though we are not focused on this problem due to different understanding from different experts, an edge map including multiple features and deduced from a training procedure can also be applied for snake based segmentation.

The time cost of our algorithm comprises many different parts. In our experimental hardware environment, CPU Intel Core i5-430M, 2 GB RAM, the proposed method implemented by MATLAB takes approximately 23 s to process all 50 images. The average time cost is 0.46 s. Based on this implementation, we find the most costly part is Hough transform, taking up to approximate 75% out of total time cost. The inefficiency can be attributed to thick edges after thresholding. Non-maxima suppression [37] can be applied to keep edges thin, with only vertical orientation considered. This reduced the time cost of Hough transform approximately by half

while occasionally introducing ill-positioned line segments. Other improvements of Hough transform such as using gradient direction from the original image [25], statistically selecting few edge points [27], or randomly choosing two points for line detection [26], can also be applied to improve the overall efficiency.

#### 4.2. Advantage and limit

The benefits of our method come from application of Hough transform in the initial contour construction and the uniform energy in the DS model. Because the Hough transform considers all the edge points in the BIS, it is less likely to be affected by noises. Its global nature also compensates the holes or missing boundaries that are common in ultrasound images. Moreover, the distance constraint and angle constraint enable detection of two nearly parallel line segments that satisfy a large thickness range. The shape constraint in the proposed DS can estimate the missing LII boundary according to the MAI contour and neighboring distances. Besides, since this prior is defined in a variational framework, sub-pixel accuracy can be achieved.

Despite the above advantages, there are two limits relating to the proposed method. Firstly, the initial contour construction relies on the assumption that the boundaries are piecewise linear curves. This means the method would work fine for early thickening IMC. However, it would fail for irregular boundaries where such assumption does not hold, e.g., plaques. In the context of plaque segmentation, the traditional DP exhibits an advantage that employs the same cost function [5]. Secondly, the proposed DS is inclined to obliterate minor details since the uniform energy tries to maintain two parallel curves with little distance variation. This disadvantage could be trivial given that with small uniform energy, general thickness variation can still be maintained, especially in the case that the interface presents a strong boundary. However, if minor details are important in some situation, the uniform energy should be minimized.

#### 4.3. Conclusion and future work

This paper proposed a snake model based ultrasound intima–media segmentation approach which uses Hough transform to construct the initial contours and incorporates a shape constraint relating to distance variation into snake model. According to our experiments, its performance exceeds current DP and snake based methods both qualitatively and quantitatively, and the results also provide similar clinical parameters to gold standard. Compared to DP based methods, the proposed method uses a robust initialization to avoid leak of weak boundaries and searches the local minimum in a continuous space to achieve sub-pixel accuracy. Compared to previous snake based method, the proposed method is robust to ultrasound artifacts, especially missing boundary. The future work will focus on improving the proposed method through theoretical analysis.

#### Conflicts of interest statement

There are no conflicts of interest that could inappropriately influence this work.

#### Acknowledgement

This work was funded by the Ministry of Science and Technology, China, under the International Cooperation Project (Grant No. 2009DFA12290).

## References

- [1] Bots ML, Hoes AW, Koudstaal PJ, Hofman A, Grobbee DE. Common carotid intima–media thickness and risk of stroke and myocardial infarction: the Rotterdam Study. *Circulation* 1997;96(5):1432–7.
- [2] O’Leary DH, Polak JF, Kronmal RA, Manolio TA, Burke GL, Wolfson SK. Carotid-artery intima and media thickness as a risk factor for myocardial infarction and stroke in older adults. *The New England Journal of Medicine* 1999;340(1):14–22.
- [3] Baldassarre D, Sci B, Werba P, Tremoli E, Poli A, Pazzucconi F, et al. Common carotid intima–media thickness measurement. *Stroke* 1994;25:1588–92.
- [4] Wendelhag I, Liang Q, Gustavsson T, Wikstrand J. A new automated computerized analyzing system simplifies readings and reduces the variability in ultrasound measurement of intima–media thickness. *Stroke* 1997;28(11):2195–200.
- [5] Liang Q, Wendelhag I, Wikstrand J, Gustavsson T. A multiscale dynamic programming procedure for boundary detection in ultrasonic artery images. *IEEE Transactions on Medical Imaging* 2000;19(2):127–42.
- [6] Cheng D, Schmidt-Trucks SSA, Cheng K, Burkhardt H. Using snakes to detect the intimal and adventitial layers of the common carotid artery wall in sonographic images. *Computer Methods and Programs in Biomedicine* 2002;67(1):27–37.
- [7] Ceccarelli M, De Luca N, Morganello A. An active contour approach to automatic detection of the intima–media thickness. In: *IEEE international conference on acoustics, speech and signal processing*. 2006. p. 709–12.
- [8] Loizou CP, Pattichis CS, Pantziaris M, Tyllis T, Nicolaides A. Snakes based segmentation of the common carotid artery intima media. *Medical and Biological Engineering and Computing* 2007;45(1):35–49.
- [9] Cheng DC, Jiang X. Detections of arterial wall in sonographic artery images using dual dynamic programming. *IEEE Transactions on Information Technology in Biomedicine* 2008;12(6):792–9.
- [10] Destrempes F, Meunier J, Giroux MF, Soulez G, Cloutier G. Segmentation in ultrasonic B-mode images of healthy carotid arteries using mixtures of Nakagami distributions and stochastic optimization. *IEEE Transactions on Medical Imaging* 2009;28(2):215–29.
- [11] Molinari F, Zeng G, Suri JS. A state of the art review on intima–media thickness (IMT) measurement and wall segmentation techniques for carotid ultrasound. *Computer Methods and Programs in Biomedicine* 2010;100(3):201–21.
- [12] Kass M, Witkin A, Terzopoulos D. Snakes: active contour models. *International Journal of Computer Vision* 1988;1(4):321–31.
- [13] Cohen LD. On active contour models and balloons. *CVGIP: Image Understanding* 1991;53(2):211–8.
- [14] Zhu SC, Yuille A. Region competition: unifying snakes, region growing, and bayes/mdl for multiband image segmentation. *IEEE Transactions on Pattern Analysis and Machine Intelligence* 1996;18(9):884–900.
- [15] Caselles V, Kimmel R, Sapiro G. Geodesic active contours. *International Journal of Computer Vision* 1997;22(1):61–79.
- [16] Xu C, Prince JL. Snakes, shapes, and gradient vector flow. *IEEE Transactions on Image Processing* 1998;7(3):359–69.
- [17] Chan TF, Vese LA. Active contours without edges. *IEEE Transactions on Image Processing* 2001;10(2):266–77.
- [18] Cremers D, Rousson M, Deriche R. A review of statistical approaches to level set segmentation: integrating color, texture, motion and shape. *International Journal of Computer Vision* 2007;72(2):195–215.
- [19] Li C, Kao C, Gore J, Ding Z. Minimization of region-scalable fitting energy for image segmentation. *IEEE Transactions on Image Processing* 2008;17(10):1940–9.
- [20] Amini A, Weymouth TE, Jain RC. Using dynamic programming for solving variational problems in vision. *IEEE Transactions on Pattern Analysis and Machine Intelligence* 1990;12(9):855–67.
- [21] Boykov Y, Veksler O, Zabih R. Fast approximate energy minimization via graph cuts. *IEEE Transactions on Pattern Analysis and Machine Intelligence* 2001;23(2):1222–39.
- [22] Boykov Y, Kolmogorov V. An experimental comparison of min-cut/max-flow algorithms for energy minimization in vision. *IEEE Transactions on Pattern Analysis and Machine Intelligence* 2004;26(9):1124–37.
- [23] Boykov Y, Funka-Lea G. Graph cuts and efficient image segmentation. *International Journal of Computer Vision* 2006;70(2):109–31.
- [24] Duda RO, Hart PE. Use of the Hough transformation to detect lines and curves in pictures. *Communications of the ACM* 1972;15:11–5.
- [25] Ballard DH. Generalizing the Hough transform to detect arbitrary shapes. *Pattern Recognition* 1981;13(2):111–22.
- [26] Xu L, Oja E, Kultanen P. A new curve detection method: randomized Hough transform (RHT). *Pattern Recognition Letters* 1990;11(5):331–8.
- [27] Kiryati N, Eldar Y, Bruckstein AM. A probabilistic Hough transform. *Pattern Recognition* 1991;24(4):303–16.
- [28] Golemati S, Stoitsis J, Sifakis E, Balkizas T, Nikita K. Using the Hough transform to segment ultrasound images of longitudinal and transverse sections of the carotid artery. *Ultrasound in Medicine & Biology* 2007;33(12):1918–32.
- [29] Stoitsis J, Golemati S, Kendros S, Nikita KS. Automated detection of the carotid artery wall in B-mode ultrasound images using active contours initialized by the Hough transform. In: *Conf. Proc. IEEE Eng. Med. Biol. Soc.* 2008. p. 3146–9.
- [30] Gunn S, Nixon M. A robust snake implementation: a dual active contour. *IEEE Transactions on Pattern Analysis and Machine Intelligence* 1997;19(1):63–8.
- [31] Zeng X, Staib L, Schultz R, Duncan J. Segmentation and measurement of the cortex from 3-D MR images using coupled-surfaces propagation. *IEEE Transactions on Medical Imaging* 2002;18(10):927–37.
- [32] Hohnhauser B, Hommel G. 3D pose estimation using coupled snakes. In: *WSCG conference proceedings*. 2004. p. 161–5.
- [33] Lynch M, Ghita O, Whelan P. Left-ventricle myocardium segmentation using a coupled level-set with a priori knowledge. *Computerized Medical Imaging and Graphics* 2006;30(4):255–62.
- [34] Zhu Y, Papademetris X, Sinusas A, Duncan J. A coupled deformable model for tracking myocardial borders from real-time echocardiography using an incompressibility constraint. *Medical Image Analysis* 2010;14(3):429–48.
- [35] Srikrishnan V, Chaudhuri S, Roy SD, Evcovic D. On stabilisation of parametric active contours. In: *IEEE conference on computer vision and pattern recognition*. 2007. p. 1–6.
- [36] Bland JM, Altman DG. Statistical methods for assessing agreement between two methods of clinical measurement. *The Lancet* 1986;327(8476):307–10.
- [37] Canny J. A computational approach to edge detection. *IEEE Transactions on Pattern Analysis and Machine Intelligence* 1986;8(6):679–98.

**Xiangyang Xu** received his B.S., M.S. and Ph.D. degrees at Huazhong University of Science and Technology (HUST), China, in 1988, 1991 and 2010, respectively. Now he is an associate professor in HUST. His research areas are signal and image processing.

**Yuan Zhou** received his B.E., M.E. degrees at School of Software Engineering, School of Computer Science and Technology, in 2008, 2011, respectively, both from Huazhong University of Science and Technology, Wuhan, China. His research interests are computer vision and medical image processing.

**Xinyao Cheng** received his bachelor’s degree from fourth military medical university in 1985, master’s degree from cardiovascular disease institute, union hospital, Tongji Medical College of Huazhong University of Science and Technology in 1990, and Ph.D. degree in biochemistry and molecular biology from medical school of Osaka university. He has been a physician in cardiology and researched on the basic and clinical cardiovascular diseases.

**Enmin Song** received his Ph.D. in 1999. He is a senior member of IEEE. He has been a professor at the School of Computer Science and Technology, Huazhong University of Science and Technology, PR China since 2004. His research interests include medical image processing and artificial intelligence.

**Guokuan Li** received the B.S. degree and M.E. degree both in automatic control engineering, Ph.D. in pattern recognition and artificial intelligence, from Huazhong University of Science and Technology, in 1993, in 1996, and in 2000, respectively. After receiving the Ph.D., he joined Imaging Research Labs, Robarts Research Institute, Canada, where he worked for 5 years, focusing on research of medical imaging and medical image processing. He joined the faculty at Huazhong University of Science and Technology, Wuhan in 2006 and is currently working as an associate professor in School of Computer Science and Technology. His research interests include stereoscopic video, digital media, image processing, analysis, and visualization, instrumentation, wavelet and computer vision.